

# European Conference on **Biomedical Optics**

22–25 June 2003

ICM—International Conference Center  
Munich, Germany

*Colocated with*

**Laser Munich 2003 - World of Photonics**

**Photon Migration and  
Diffuse-Light Imaging**

**Confocal, Multiphoton, and  
Nonlinear Microscopic Imaging**


**Optical Coherence Tomography  
and Coherence Techniques**

**Diagnostic Optical Spectroscopy**

**Therapeutic Laser Applications  
and Laser-Tissue Interactions**

**Novel Optical Instrumentation for  
Biomedical Applications**

*Sponsored by:*

 **SPIE** The International Society  
for Optical Engineering

  
Optical Society of America

# Conference 5143 • Room: 11 (Tues); 5 (Wed)

## SESSION 4

Room: 5 ..... Wed. 14.00 to 16.00

### Methods and Instruments II

Chair: Serge R. Mordon, INSERM Lille (France)

11.00: **Advantages of holographic optical tweezers**, M. Reicherter, J. Liesener, T. Haist, H. J. Tiziani, Univ. Stuttgart (Germany) ..... [5143-15]

In the last decade optical tweezers became a novel tool in microbiology. However, the setup becomes very complex if more than one trap needs to be moved. The holographic optical tweezers offer a very simple and cost efficient way of manipulating several traps independently in all three dimensions with an accuracy of less 100 nm. No mechanically moving parts are used therefore making it less vulnerable to vibration. It uses computer-generated holograms (CGHs) written into a spatial light modulator (SLM) to control the position of each trap in space and to manipulate their shape. The ability to change the shape of the optical trap makes it possible to adapt the light field to a specific particle shape or in the case of force measurements to adjust the trapping potential.

11.15: **Stochastic analysis of speckle in back-scattering**, S. Guyot, M. Péron, E. Deléchelle, Univ. Val-de-Marne (France) ..... [5143-16]

In this paper, we propose a new approach of the speckle statistics in backscattering. Applicate the Brownian motion theory to the speckle permit us to extract stochastic parameters to characterize it. It seems more powerful than the classical frequential approach to characterize and classify speckle. We present an application of this method on a test media.

11.30: **Non-invasive polarimetric glucose measurement system for eye phantoms and in-vivo measurement requirements**, R. C. Rawer, P. Vollmer, C. Unkrich, W. Stork, K. D. Müller-Glaser, Univ. Karlsruhe (Germany) ..... [5143-17]

Non-invasive monitoring of the glucose level is a key technology for improved diagnosis and therapy for Diabetes patients. Optical measurement techniques like polarimetry measuring at the human eye offer promising properties for non-invasive and painless application. This article presents a polarimetric measurement system utilizing the polarizing properties of the Aqueous Humour (AH) for quantitative glucose measurements at eye phantoms. It also discusses the special requirements of in-vivo measurements for such a system.

11.45: **Mueller polarimetric system and matrix decomposition schemes for biomedical applications**, B. Laude, Ecole Polytechnique (France); S. Guyot, B. Clairac, Univ. Val-de-Marne (France); A. De Martino, E. Garcia Caurel, Ecole Polytechnique (France); L. Schwartz, Hôpital Pitié Salpêtrière (France); B. Drévilion, Ecole Polytechnique (France) ..... [5143-18]

We present a new Mueller polarimetric system based on liquid crystal modulators, together with original Mueller matrix decomposition schemes providing interesting contrast mechanisms. The instrument design, together with an original an easy-to-operate calibration procedure, provides a high measurement accuracy over a wide spectral range. The raw data are taken either with a single detector or a CCD camera and are processed with different algorithms. Results obtained with various samples of biological interest will be discussed.

12.00: **Polarimetric glucose sensing using Brewster-reflection off the ocular lens applying a rotating retarder analyzer**, S. Böckle, Univ. degli Studi di Brescia (Italy); L. L. Rovati, Univ. degli Studi di Modena e Reggio Emilia (Italy); R. R. Ansari, NASA Glenn Research Ctr. (USA) ..... [5143-19]

We propose a polarimetric method that exploits the Brewster-reflection off of the eye lens to perform glucose sensing. After reflection, the resulting linearly polarized light is rotated by the glucose molecules in the aqueous humor, thus carries the glucose concentration information. A proof-of-concept experimental setup is presented applying a multi-wavelength true-phase measurement approach and a rotating phase retarder as an analyzer to measure the small rotation angles and the complete polarization state of the measurement light.

12.15: **Magneto-optical study of anisotropic magnetic properties of biomicroparticles containing reactive oxygen species or ferritin**, S. B. Norina, Moscow State Univ. (Russia) ..... [5143-20]

Speckle based and laser diffusion methods combined with pulsating weak magnetic field 1-5 Hz were applied to observe resonant vibrations of biological microparticles with anisotropic magnetic properties. Modeling of oxidative disorders in tissues was realized using reactive oxygen species (ROS) initiation and ferritin incorporation into porous sorbent beads and blood cells. Microscopic video recording of cells in high gradient magnetic separation allowed to determinate changes of magnetic moments under stress-activating influences.

Lunch Break ..... 12.30 to 14.00

14.00: **Cells and tissue imaging with digital holographic microscopy**, C. D. Depeursinge, E. Cuhe, T. Colomb, P. Massatch, A. Marian, F. Montfort, Ecole Polytechnique Fédérale de Lausanne (Switzerland); P. Marquet, P. Magistretti, Univ. de Lausanne (Switzerland) ..... [5143-21]

The aim of Optical Digital Holography, applied to cells and tissue imaging, is to provide an accurate 3D imaging of biologic materials, down to the microscopic scale. The method has been developed to yield a very precise determination of cells and tissues morphology. Targeted accuracies are in the sub-micron range and allow for the observation of very small movements and deformations, produced, in particular, by depolarization of excitable cells and their metabolic activities. Direct imaging of tissue structures by the newly developed digital holography is deemed to offer unique investigation means in biology and medicine and attractive diagnostic capabilities.

14.15: **Fluorescence apertureless scanning near-field microscopy for high resolution biological imaging**, A. Fragola, L. Aigouy, ESPCI (France) ..... [5143-22]

Apertureless scanning near-field optical microscopy (SNOM) offers new opportunities in fluorescence imaging by providing subwavelength resolution. This is achieved by scattering the near-field with a metallic tip. SNOM images have been recorded on fluorescent spheres and erbium-doped vitroceraimic. We will also present approach curves that allow to better understand the near-field optical contrast origin. Our near-field microscope is now suitable for immersed samples imaging, in order to study biological samples.

14.30: **Imaging of functional brain activation using laser speckle and imaging of functional brain activation using laser speckle and spectral imaging**, A. K. Dunn, Massachusetts General Hospital (USA) and Massachusetts General Hospital (USA) and Harvard Medical School (USA); A. Devor, M. Andermann, A. Dale, D. Boas, Massachusetts General Hospital (USA) ..... [5143-23]

By combining laser speckle contrast imaging with spectral imaging, the blood flow, total hemoglobin and oxygenation changes in the brain can be imaged during functional activation. We present images of changes in blood flow, hemoglobin concentration and CMRO<sub>2</sub> in response to rat whisker stimulation.

14.45: **Development of a novel optical biopsy system combining optical-fiber reflectance confocal imaging and confocal autofluorescence spectroscopy**, M. Genet, Mauna Kea Technologies (France); S. Villette, G. Bourg-Heckly, Univ. Pierre et Marie Curie (France); S. Loiseau, Mauna Kea Technologies (France) ..... [5143-24]

The coupling of fibered confocal imaging and autofluorescence spectroscopy will enable a multimodal observation consisting of morphological information at a cellular level and biochemical data given by the spectral signatures of the tissues. We are developing such a dual system, which provides in real time the reflectance image (at 685 nm) and the autofluorescence spectrum (excited at 405 nm) of the same optical section located at a depth of up to 100 microns.

15.00: **Laser-scanning endoscope based on polysilicon micromachined mirrors with enhanced attributes**, M. George, Eberhard-Karls-Univ. Tübingen (Germany); H. Albrecht, Laser- und Medizin-Technologie GmbH (Germany); M. Schurr, Eberhard-Karls-Univ. Tübingen (Germany); P. G. Papageorgas, Univ. of Athens (Greece); U. Hofmann, Fraunhofer-Institut für Siliziumtechnologie (Germany); D. Maroulis, Univ. of Athens (Greece); C. D. Depeursinge, Swiss Federal Institute of Technology (Switzerland); D. Iakkovidis, N. Theofanous, Univ. of Athens (Greece); A. Menciasci, Scuola Superiore Sant Anna (Italy) ..... [5143-25]

Usual endoscopic systems provide a continuous vision of otherwise inaccessible regions during medical operations or diagnosis procedures. A laser-scanning endoscope device has been developed aiming to provide superior resolution and chromatic representation in comparison with commercial endoscopes. The scanning operation of the laser beams used in this endoscope device relies on tiny microelectro-mechanical silicon mirrors. This microscanning endoscope system provides color imaging with high resolution at near video rates targeting at macroendoscopy applications.

Order Proceedings now and take advantage of the special prepublication price: \$80

Proceedings of SPIE Volume 5143

See p.37 to order.

# A laser-scanning endoscope based on polysilicon micromachined mirrors with enhanced attributes

George M.<sup>a</sup>, Albrecht H.<sup>b</sup>, Schurr M. O.<sup>a</sup>, Papageorgas P.<sup>c</sup>, Hofmann U.<sup>d</sup>, Maroulis D.<sup>c</sup>,  
Depeursinge C.<sup>e</sup>, Iakkovidis D.<sup>c</sup>, Theofanous N.<sup>c</sup> and Menciassi A.<sup>f</sup>

<sup>a</sup>University of Tübingen, Waldhörnlestraße 22, 72072 Tübingen, Germany

<sup>b</sup>LMTB gGmbH, Fabeckstraße 60–62, 14195 Berlin, Germany

<sup>c</sup>University of Athens, Panepistimiopolis, Ilissia, 15784 Athens, Greece

<sup>d</sup>Fraunhofer Institute for Silicon Technology, Fraunhoferstraße 1, 25524 Itzehoe, Germany

<sup>e</sup>Ecole Polytechnique Fédérale de Lausanne, 1015 Lausanne, Switzerland

<sup>f</sup>Scuola Superiore Sant'Anna, Piazza Martiri della Libertà 33, 56127 Pisa, Italy

## ABSTRACT

A miniaturized laser scanning endoscope is presented which makes use of three lasers to illuminate a sample with a red, a green and a blue wavelength simultaneously. Scattered light from the sample is descanned and chromatically separated into the three channels for detection and postprocessing to compose a color image. The scanning subsystem consists of two micro-electro-mechanical mirrors suitable for mass production. The endoscope head can be assembled fast and at low cost. A resolution of the order of 16 lines per mm is achieved for a working distance common in endoscopy. Considerations of the system design include the operation of the micro mirrors, the filtering of reflected light by using polarization effects and a strategy to cope with color metamery. An expert system based on a neural network was found able to analyze endoscopic images to identify suspicious lesions.

**Keywords:** laser scanning, endoscope, silicon micromirror, MEMS, color metamery, expert system, neural network

## 1. INTRODUCTION

Medical endoscopes in clinical use today<sup>1,2</sup> employ CCD or CMOS sensors for video imaging in NTSC or PAL mode. For illumination, optical fiber bundles transfer the light from specialized sources to the tip of the endoscope. Fiber bundles can also be used for detection, but in advanced endoscopes the sensor arrays are integrated in the tip. However, for a common working distance the achievable resolution will be limited by the video mode resolution.

As an alternative approach, a laser scanning endoscope will be presented here. Due to the image formation based on a scanning beam, the resolution is limited by the optical properties of the endoscope only. The system comprises a three color laser illumination, an endoscopic scanning probe, a three color detection unit and a software package for instrument control and real time image processing and visualization. The recorded images can also be fed into an neural network expert system for image analysis. The latter feature can assist in the detection of early lesions in the gastrointestinal tract.

After describing key considerations for the design of the system, the imaging performance will be assessed, and its advantages and drawbacks will be discussed. The operation of the neural network expert system will be demonstrated based on images provided by standard video colonoscopy.

---

Send correspondence to M.G. or N.T.

Markus George: E-mail: info@markus-george.de, Telephone: +49 7071 29-81249

Nikiforos Theofanous: E-mail: optel@di.uoa.gr, Telephone: +30 210 727-5303

## 2. SYSTEM COMPONENTS AND OPERATION

The scanning endoscope system (figure 1) consists of the illumination unit with the three laser sources, the endoscope head, the detection unit based on three avalanche photo diodes connected to a computer for data acquisition, a computer-controlled high voltage supply to provide the drive voltages for the scanning mirrors and the computer software which controls the synchronised action of all parts and displays a color image on screen.

### 2.1. Scanning Endoscope Head

The endoscope head (figure 2) is the core of the system and has a diameter of 12.5 mm. Its optical components contain fibers for illumination and detection with collimating microlenses, a unit consisting of two polarizing beam splitters and a prism for beam deflection, the micromachined scanning mirrors and an optical window.

The micromachined scanners are similar to scanner setups described before<sup>3-5</sup> and are driven electrostatically. They consist of a silicon mirror which is suspended via a nickel microspring axis inside a silicon frame. This wet-etched structure is mounted with an appropriate distance onto a pyrex substrate with two integrated electrodes and connector terminals. The electrodes are oriented in parallel to the mirror axis, so that each electrode is below one half of the mirror. For operation, a positive voltage  $U_{\text{drive}}$  is applied to one electrode and a negative voltage  $-U_{\text{drive}}$  of the same amount to the other electrode, while the mirror remains grounded or biased with the voltage  $U_{\text{bias}}$ . The resulting electrostatic force between each electrode and the mirror cause two torques

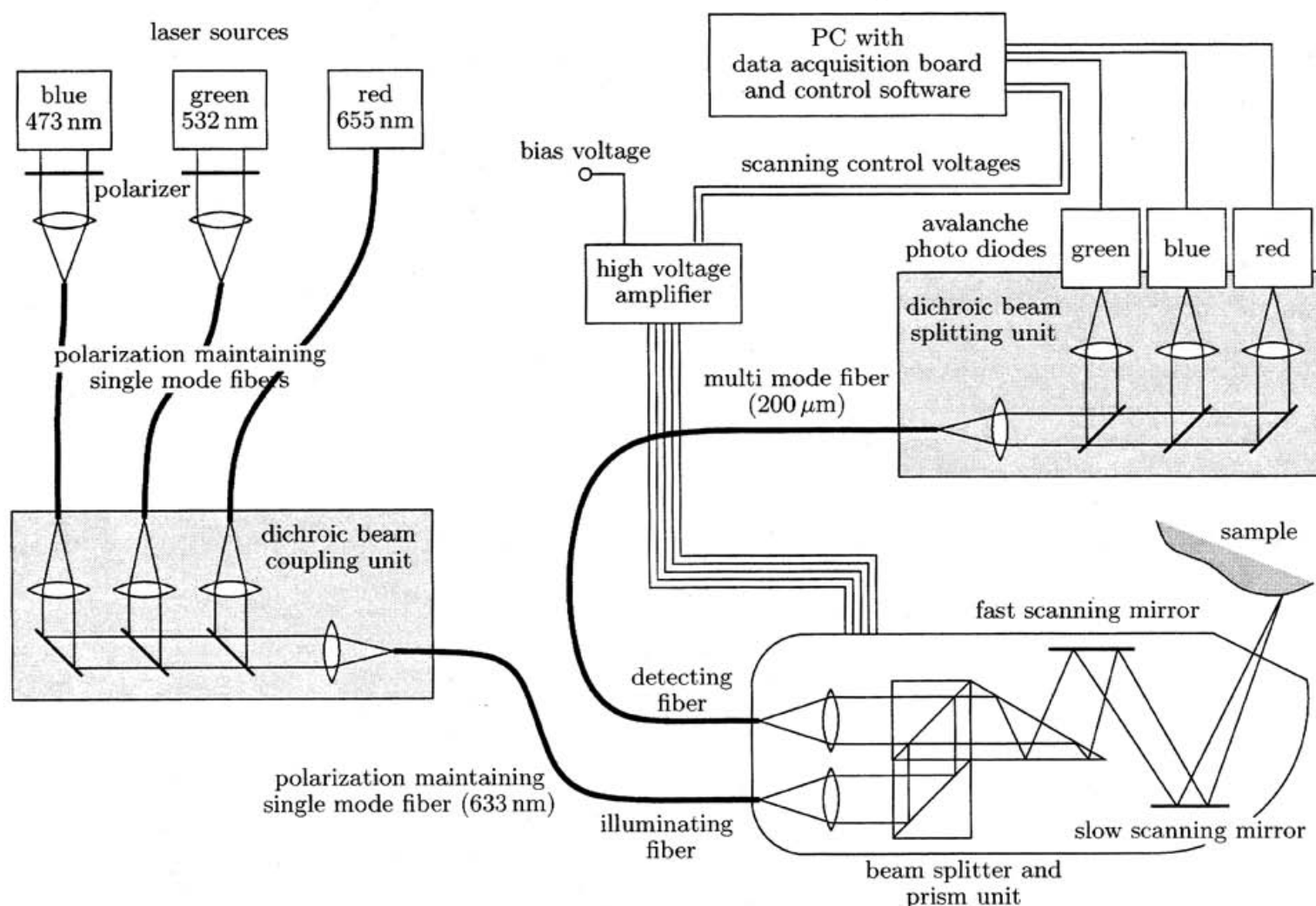


**Figure 1.** System for three-color laser scanning endoscopy. The three laser wavelengths are provided through a polarization maintaining fiber to the endoscope for illumination. The backscattered light is led by a multimode fiber to the detection unit.



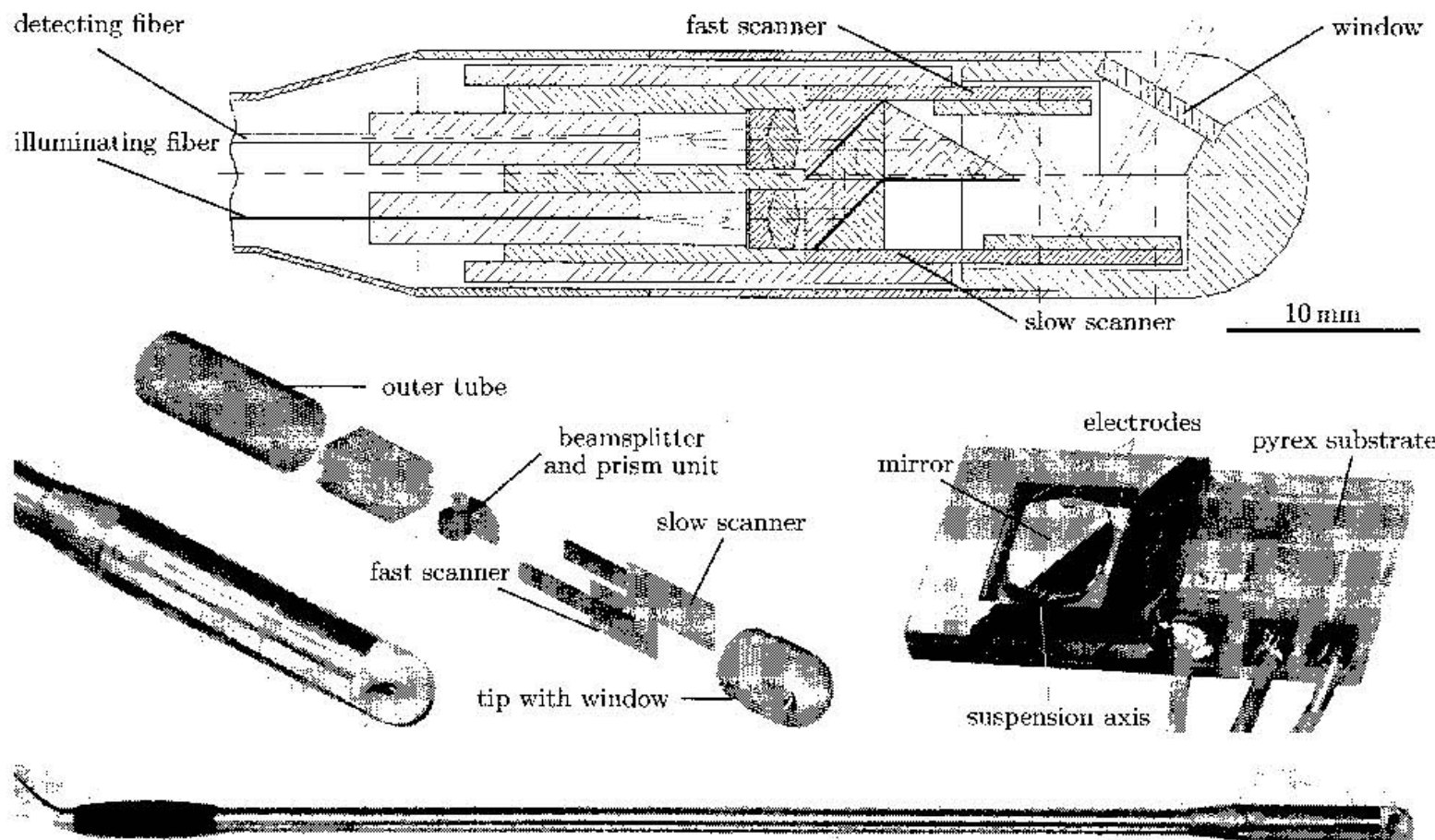


**Figure 2.** Top: Optomechanics of the scanning endoscope head. Center from left to right: Photograph of the assembled head, schematic of the subcomponents of the head and photograph of the micromachined mirror for the fast scanning axis. Bottom: Complete endoscope.

$|M_1| \propto (U_{\text{bias}} - U_{\text{drive}})^2$  and  $|M_2| \propto (U_{\text{bias}} + U_{\text{drive}})^2$  respectively. The total torque

$$M_{\text{total}} = M_2 - M_1 \propto (U_{\text{bias}} - U_{\text{drive}})^2 - (U_{\text{bias}} + U_{\text{drive}})^2 = 4 U_{\text{bias}} U_{\text{drive}} \quad (1)$$

is no longer proportional to the square of the drive voltage. Obviously, by applying a non-zero bias voltage the relation between the applied voltage and the mirror deflection angle can be linearized.<sup>5</sup> The amplitude of  $U_{\text{drive}}$  ranges from 100 V to 400 V depending on the bias voltage setting and the required field of view.

The fast scanner is generally driven resonantly, and different scanners with frequencies between 500 Hz and 1.2 kHz were tested. In contrast, the slow scanner has a resonant frequency around 50 Hz and is operated quasi-statically. The image acquisition time depends on the frequency of the fast scanner and is between 1 s and 2.5 s. The resonant frequency of a scanning mirror is defined by its mass and the stiffness of the spring suspension. The higher the resonant frequency, the lower the mirror deflection achieved for a given driving voltage amplitude. As a result, there is a tradeoff between the image acquisition speed and the field of view.

The arrangement of the mirrors is crucial for maximizing the achievable field of view. Each mirror is capable to perform a rotation of about  $\pm 2.5^\circ$  around its axis, which would enable a beam deflection of  $\pm 5^\circ$  for a beam incident perpendicular onto the non-rotated mirror. This condition cannot be realized in a miniaturized endoscope head, however the angle of incidence onto the scanner was kept as perpendicular as possible by using a prism for beam deflection.

The endoscope head is mounted on a rigid tube to form a total length of approximately 50 cm. The whole endoscope, especially the head, has been designed so that it can be assembled easily and that its components, including the silicon wet-etched mirrors, are suitable for mass production.

## 2.2. Image Formation Based on Backscattered Light

The endoscope detects primarily light backscattered from the object rather than direct Fresnel reflection from the sample surface. This is necessary, as the endothelium is naturally covered by a liquid film during examination, the reflection of which does not carry any information on the tissue. Another advantage is that scattered light also carries information about layers below the tissue surface. Thus, the laser scanning endoscope becomes a multi-wavelength measurement tool for elastic light scattering. The rejection of Fresnel reflection is achieved by using a linearly polarized illumination and removing the light of this polarization in the detection path, which is done using a polarization dependent beam splitter in front of the collimating lens to the detecting fiber.

Therefore, polarized illumination has to be chosen. The red diode laser source (655 nm) provides a polarized output directly, while the frequency-doubled diode-pumped solid state lasers for the green (532 nm) and blue (457 nm) wavelengths have to be beam-shaped and polarized before being coupled into the optical fiber.

In the diffusion regime, i.e. when scattering dominates absorption, the backscattering can be estimated easily. The total amount of backscattered light is<sup>6</sup>

$$R_{\text{total}} = \frac{a}{2} \left( 1 + \exp \left( -\frac{4}{3} A \sqrt{3(1-a)} \right) \right) \exp \left( -\sqrt{3(1-a)} \right), \quad (2)$$

where  $a$  is the albedo and  $A$  a parameter describing the internal reflection which depends on the refractive index. More important, the radial dependence of the amount of backscattered light  $R^{2\pi}(r)$  into the half sphere can be calculated as

$$R^{2\pi}(r) = \frac{a}{2\pi} \left( \frac{1}{\mu_t} \left( \mu_{\text{eff}} + \frac{1}{r_1} \right) + \left( \frac{1}{\mu_t} + 2z_b \right) \left( \mu_{\text{eff}} + \frac{1}{r_2} \right) \frac{\exp(-\mu_{\text{eff}} r_2)}{r_2^2} \right), \quad (3)$$

where  $\mu_{\text{eff}}$  is the effective attenuation coefficient,  $\mu_t$  total interaction coefficient,  $r_1$  and  $r_2$  the positions of two light sources simulating a semi-infinite medium and a pencil beam illumination, and  $z_b$  describing the effect of reflection at the boundary. These calculations provide only an estimate because the diffusion theory is simplified and only valid in the range where scattering strongly dominates absorption. Thus, due to the chromatic dependence of  $\mu_{\text{eff}}$  and  $\mu_t$  the amount of light backscattered from a circular region of radius  $r$  around the illuminating spot is not the same for all wavelengths. Obviously, the imaging sensitivity for each channel depends on the radius of the region from which light is collected: If the detection region is small, only a small amount of the total backscattered light is detected. As for scanner systems the resolution of the image depends mainly on the illuminated spot size, a large detection region on the object plane can be chosen to increase sensitivity. In the realized endoscopic head a detecting fiber of a 200  $\mu\text{m}$  core diameter is used leading to a detection region of 2 mm diameter in the object plane.

In endoscopy the imaged object must be at a distance  $l_{\text{obj}}$  of up to 50 mm to the imaging optic. At the same time the size of the mirrors limits the beam diameter  $D$ , so that the corresponding numerical aperture  $N.A.$  is small. The amount of light  $R^\Omega$  backscattered into the small angle  $\Omega$  can be calculated from the amount  $R^{2\pi}$  backscattered into the half sphere (equation 3) assuming isotropic backscattering:

$$R^\Omega(r) = R^{2\pi}(r) \frac{(N.A.)^2}{2} = R^{2\pi}(r) \frac{D^2}{8 l_{\text{obj}}^2} \quad (4)$$

In the endoscopic head a  $N.A. = 0.015$  could be realized and with an object distance of  $l_{\text{obj}} = 50 \text{ mm}$  the backscattered light from tissue is in the order of  $R^\Omega = 0.5 \cdot 10^{-4}$ . The amount of backscattered light emerging from a  $N.A.$  of 0.015 was also calculated by Monte Carlo simulation. Both methods provide similar results.

In addition to the loss of light caused by absorption and backscattering in the imaged object, there are significant losses on the illumination path on the way from the laser to the imaged object and also on the detection path back to the detector (table 1). The wavelength dependent reflectivity of the two scanning mirrors plays a major role, since losses at the mirror surfaces occur both in the illumination and the detection path. Further problems are the coupling efficiencies into the monomode fibers.

**Table 1.** Experimentally measured or calculated transmission coefficients for the illumination path from the laser source to the tissue surface and the detection path from the tissue to the photo detector. At the bottom of the table the resulting power balance is given. The object under observation was skin for  $N.A. = 0.015$  and a 2 mm spot diameter. The conversion gain of the detector corresponds to an avalanche photo diode module with 100 kHz bandwidth.

illumination path from laser to sample				detection path from sample to photo detector			
wavelength [nm]	650	532	457	wavelength [nm]	650	532	457
polarisation, beam shaping	1	0.5	0.34	polarisation	0.5	0.5	0.5
fiber coupling	0.9	0.15	0.44	endoscopic head	0.3	0.2	0.1
beam coupling unit	0.9	0.7	0.7	detecting fiber coupling	0.7	0.7	0.7
illumination fiber coupling	0.5	0.2	0.2	beam splitter unit	0.9	0.8	0.7
endoscopic head	0.3	0.2	0.1	gain of avalanche diode	0.7	0.4	0.3
depolarisation loss	1	0.9	0.67				
total transmission $\tau_{ill}$	0.12	0.0019	0.0014	total transmission $\tau_{det}$	0.066	0.022	0.007
laser power [mW]	10	100	100	$R^\Omega [10^{-4}]$	0.81	0.56	0.67
power on tissue [mW]	1.2	0.19	0.14	$\tau_{det} R^\Omega [10^{-6}]$	5.4	1.02	0.49
				voltage for $1.5 \cdot 10^8 \frac{V}{W}$ [mV]	1100	20	7

### 3. IMAGING RESULTS

#### 3.1. Analysis and Correction of Field Distortions

The properties of the scanners and their geometrical layout inside the scanning head introduce a moderate distortion into the image even after correcting for the sinusoidal motion of the fast scanning mirror. This distortion is demonstrated in the image of a regular, rectangular dot pattern (figure 3, left).

To be able to correct the distortion by image post-processing, for each object point  $P_o(x_o, y_o)$  the corresponding distorted image point  $P_i(x_i, y_i)$  was determined with an algorithm. With this data, two bicubic spline interpolating surfaces were calculated through the set of  $x_i$  and  $y_i$  respectively. Then for a given image coordinate

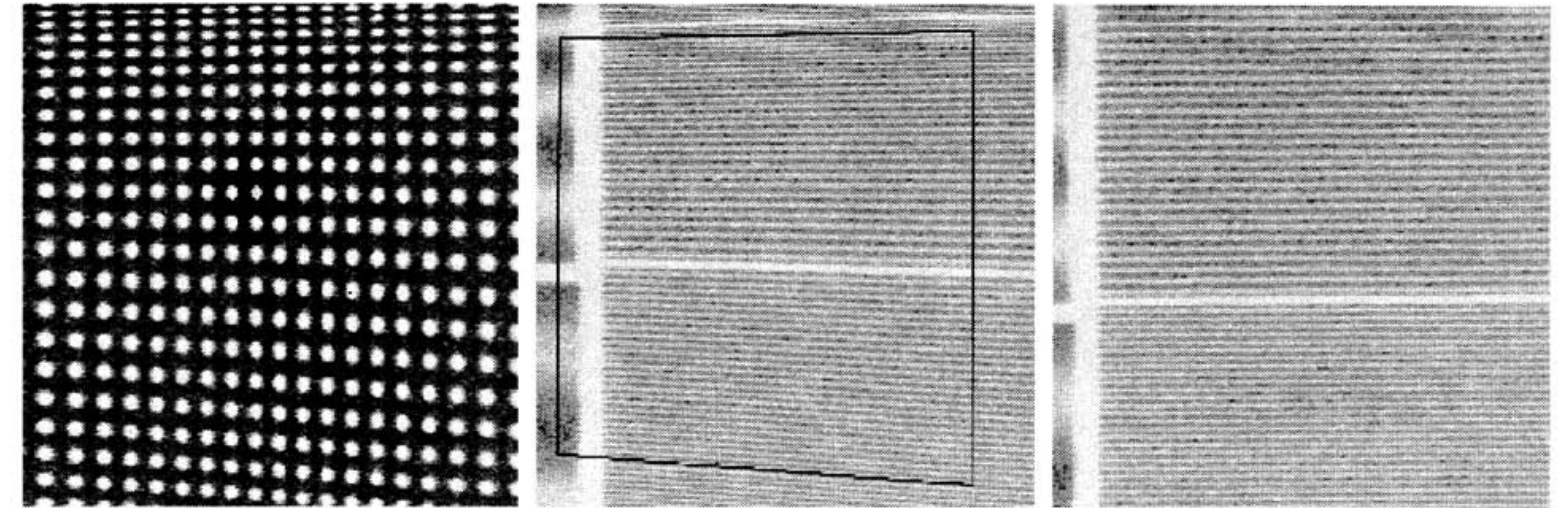


**Figure 3.** Left: Rectangular dot pattern imaged with the endoscope showing trapezoidal distortion. The diameter of each dot is 0.25 mm and the dot spacing is 0.5 mm. Center: Distorted line pattern as recorded with the endoscope. Right: The same line pattern after removing the trapezoidal distortion mathematically.



the corresponding undistorted object coordinate can be computed and vice versa. The undistorted image can then be computed by interpolating the recorded pixel array in an appropriate way.

This technique was applied on an image of a line pattern (figure 3 center) and was able to remove the trapezoidal distortion successfully (figure 3, right).

### 3.2. Modulation Transfer Function

The modulation transfer function of the endoscope was measured using a set of sinusoidal line patterns of different spatial frequencies for different target distances  $l_{obj} \approx 50$  mm around the focal length for the central region of the image (figure 4). The line pattern could be parallel or perpendicular to the fast scanning direction, resulting in the horizontal and vertical modulation transfer function respectively.

Most notably, the contrast is generally very low and lies under 0.5 even for low spatial frequencies. This low contrast is certainly due to a weak signal, resulting itself from insufficient light collected due to the small numerical aperture. The contrast should be close to 1 at low spatial frequencies with a good signal.

It can also be seen on both graphs, that at low spatial frequencies, the shorter the target distance is, the higher the contrast is (figure 5, left). At higher spatial frequencies, the highest contrast lies near the focal distance of 50 mm. For low spatial frequencies, the contrast is not much affected by defocusing, and is possibly much more dependent of the amount of collected light, which is significantly higher at short target distances. For higher spatial frequencies, focusing becomes prevalent compared to the different parameters, so that for high spatial frequencies a maximum contrast around the focal length is observe. For optimal focusing a maximum detail resolution of 16 lines per mm is achieved.

As the image is obtained by scanning horizontally the target, the modulation transfer function differs for horizontal and vertical structures. The difference between horizontal and vertical MTFs is due to a scanning synchronization problem. The image is acquired line per line, one line acquired from left to right and the next one from right to left. Although left scans and right scans are regularly synchronized, they present a little shift. This shift does not affect horizontal resolution, but affects seriously the vertical resolution (figure 5, right).

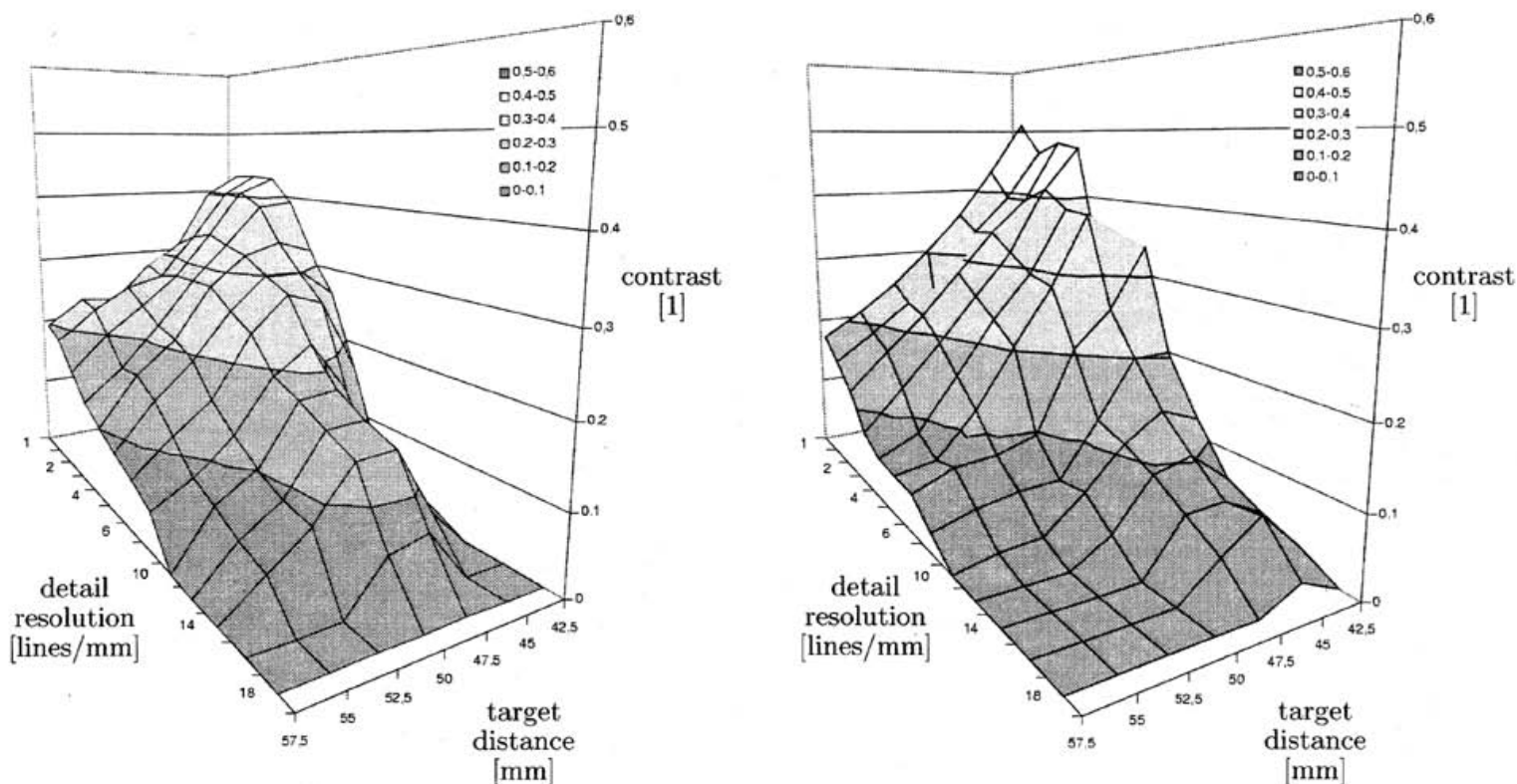
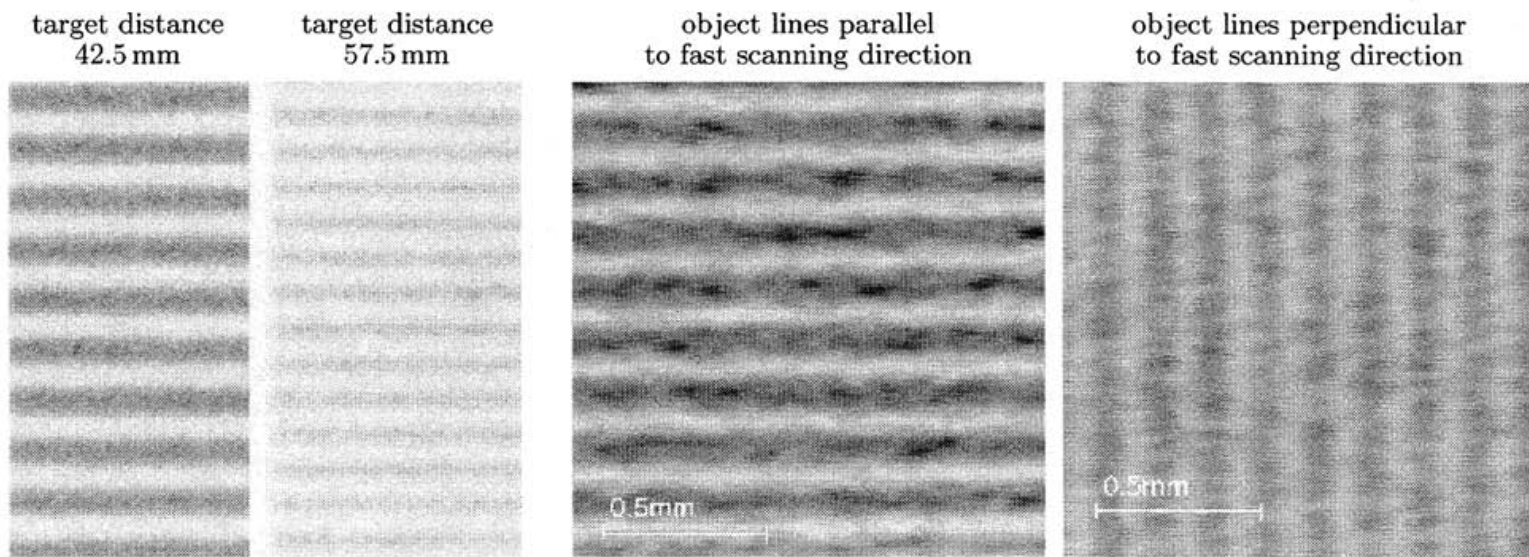


Figure 4. Left: Horizontal modulation transfer function. Right: Vertical modulation transfer function.





**Figure 5.** Left: Sinusoidal line pattern with a spatial frequency of 1.5 lines per mm at different object distances. Right: Another test pattern in horizontal and vertical orientation. The suboptimal synchronization between the horizontal fast forward and backward movement of the scanning beam deteriorates contrast.

### 3.3. Resolution Deterioration Caused by Mirror Oscillations

While the fast mirror is driven in resonance and thus performs a harmonic movement, the slow mirror is operated quasi-statically, so that the movement corresponds to the control voltage pattern applied. Mathematically, the ideal signal form for the control voltage of the slow mirror is a triangle wave for bidirectional image acquisition and a sawtooth wave for unidirectional image acquisition. However, care has to be taken since rapid changes of the control voltage derivative can excite eigen-oscillations of the slow mirror which would reduce the vertical resolution (figure 6). Luckily, for a triangular waveform these oscillations can be avoided nearly completely by an adequate choice of the bias voltage.

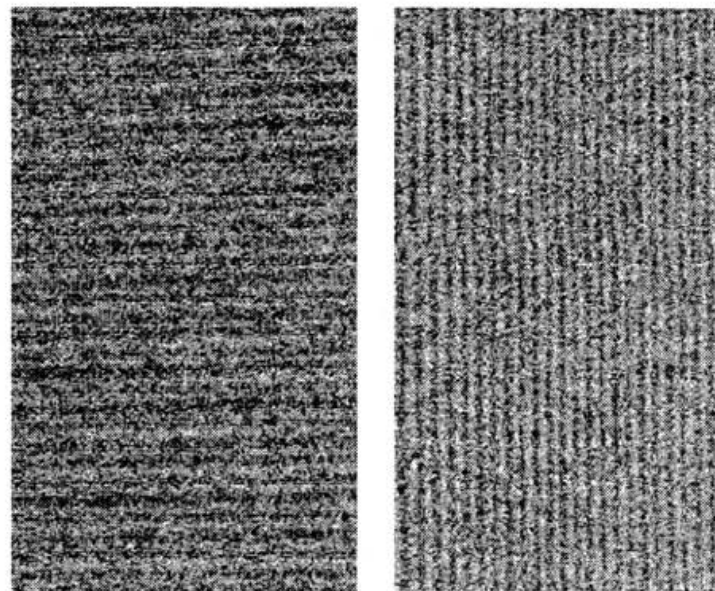
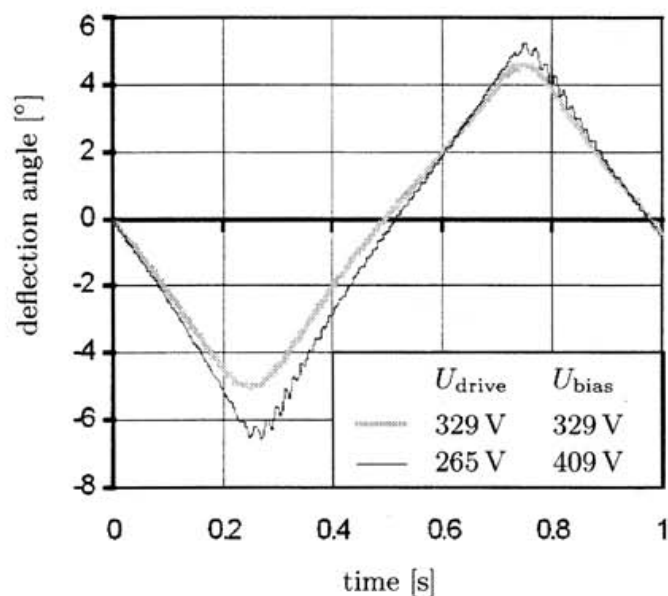


**Figure 6.** The resolution along the slow scanning direction can be deteriorated by mirror oscillations. Left: Rotation of the slow scanning mirror while being addressed by a triangular control voltage. The rapid change in direction excites the resonance of the mirror, which leads to an oscillation. Right: The excited oscillation for a sawtooth drive voltage causing the resolution in the slow scanning direction to be worse than in the fast scanning direction. The object is a Ronchi grating with 12.5 lines per mm.

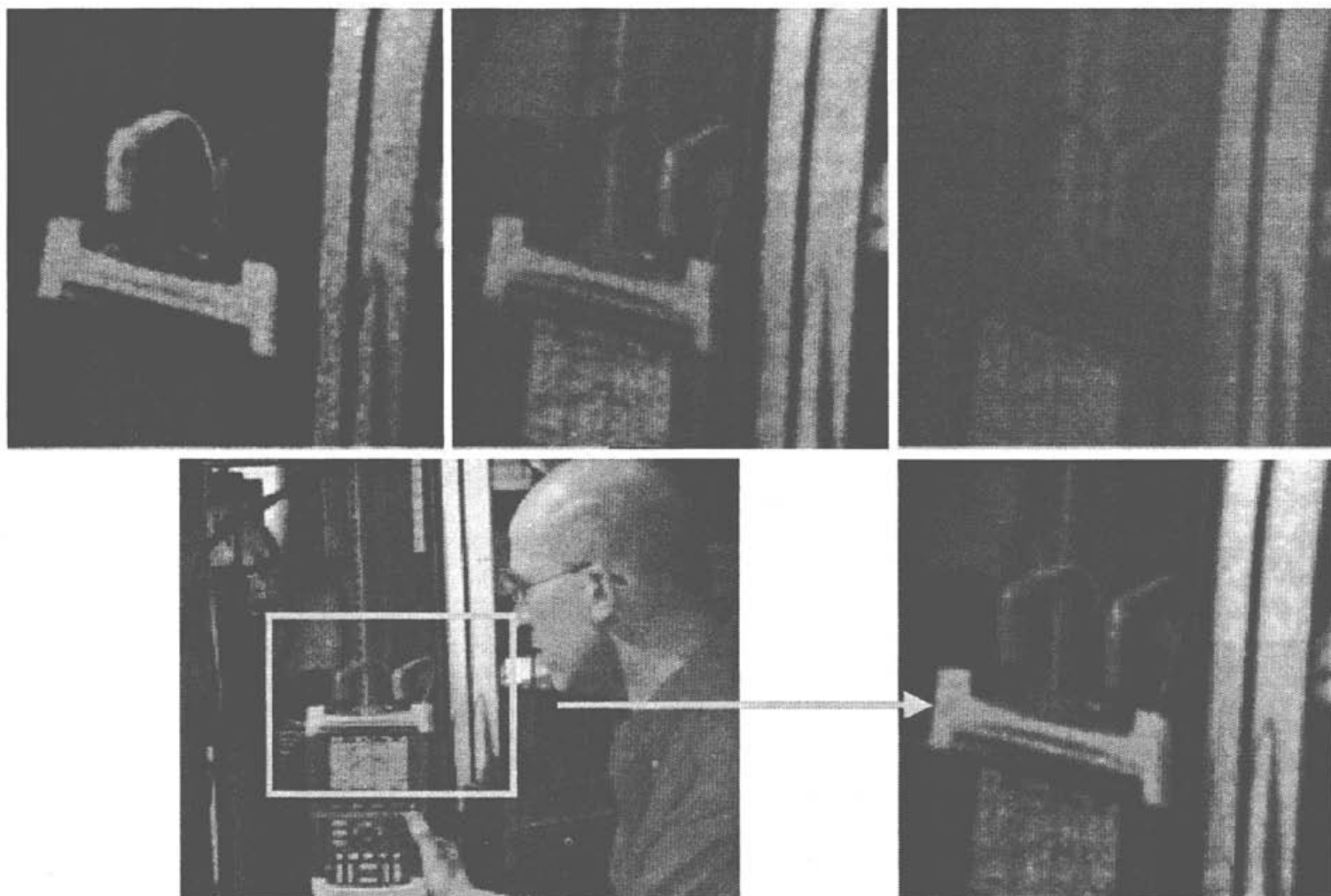


**Figure 7.** Bottom left: Color photography with a marked region of interest of  $18\text{ mm} \times 15\text{ mm}$ . Bottom right: Region of interest as composed from the three channels of the color laser scanning endoscope after gray value equalisation. Top from left to right: Sequentially recorded channels for the red, green and blue laser.

### 3.4. Imaging Technical and Biological Objects

Since the contrast achieved with the endoscope is limited due to the low numerical aperture (section 3.2), imaging of samples with little color or brightness variations tends to be difficult. Best results are obtained for technical objects. In an example (figure 7) the powers emerging from the illuminating fiber were 8 mW, 5 mW and 8 mW for the red, green and blue channel respectively, leading to powers at the object plane of 1.25 mW, 1 mW and 0.75 mW. The resulting voltage levels finally provided by the avalanche photo diodes were about 2.7 V, 400 mV and 150 mV. As expected (table 1), the efficiency of the blue channel is worst.

However, imaging biological objects is also possible (figure 8). The working distance can be adjusted by moving the ends of the illuminating and detecting optical fibers inside the endoscope head axially. The field of view enlarges geometrically as the focal distance is prolonged (figure 8, right). Moving the focus closer to the endoscope increases the numerical aperture and thus the contrast.

## 4. IMAGE PROCESSING CONSIDERATIONS

### 4.1. Color metamery

The human eye has three types of receptors which are sensitive in the continuous wavelength ranges around the blue, green and red region of the spectrum, respectively. The spectrum of the color under observation stimulates the receptors, the responses of which are processed by the brain to form the color impression. Different stimulations can lead to the same color impression, the corresponding spectral power distributions of which are

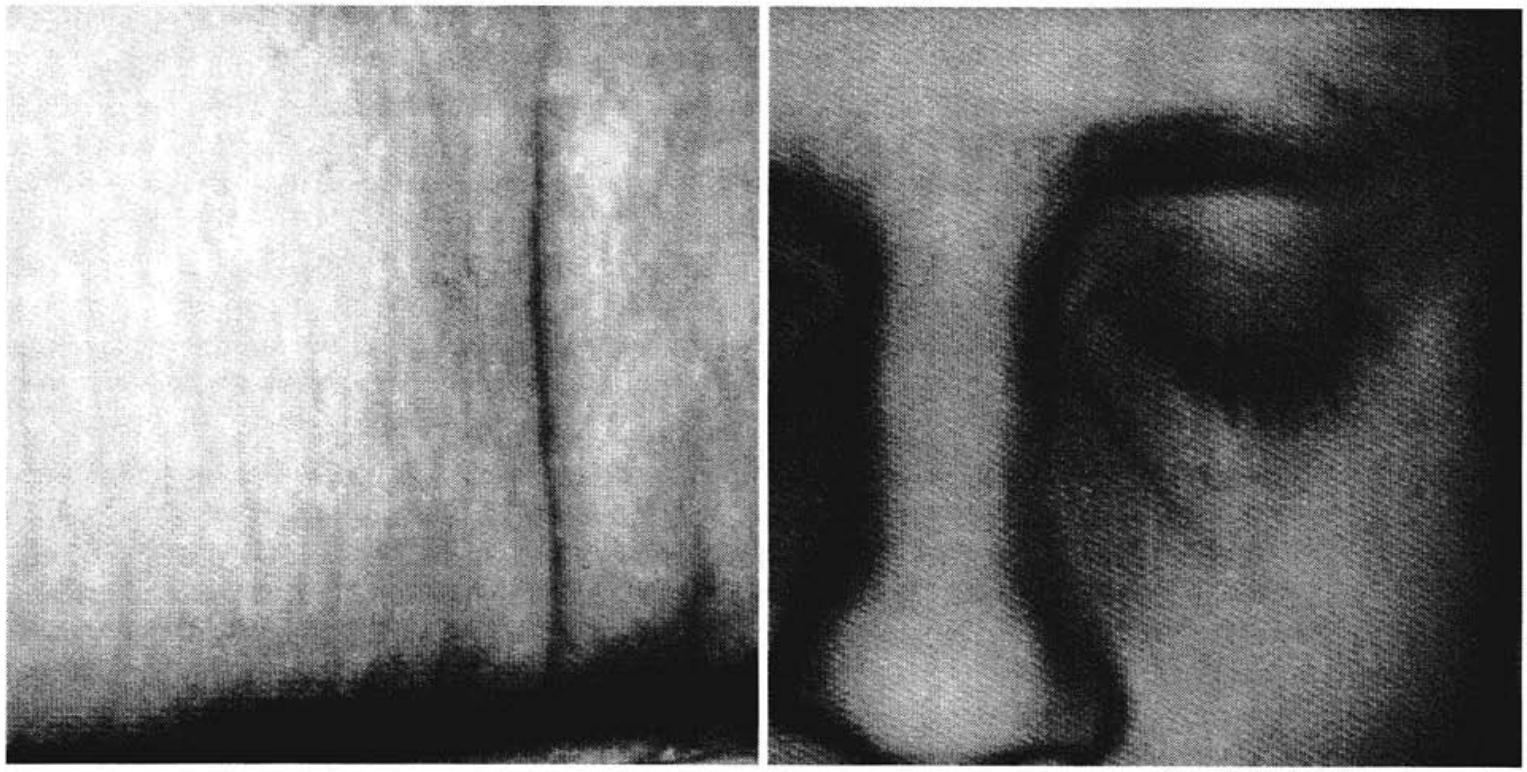


**Figure 8.** *In vivo* images of  $1024 \times 1024$  pixels recorded with the laser scanning endoscope using the 650 nm channel. The laser power in the object plane was 3 mW. The image was post-processed by a gray value equalisation. Left: Finger tissue, field of view  $12\text{ mm} \times 10\text{ mm}$ . Right: Using the same set-up, imaging at longer object distances is possible. The  $80\text{ mm} \times 80\text{ mm}$  part of the face was acquired at an object distance of about 500 mm.

denoted as metameric pairs. Since the laser scanning endoscope can evaluate only three points of the spectrum, it will be analyzed whether a satisfying color reproduction is possible.

The CIE 1931 concept of the standard observer is commonly employed for color measurement.<sup>7</sup> The spectral information of the light back-scattered or reflected from the surface under test is evaluated to form the three tristimulus values  $X$ ,  $Y$  and  $Z$ , which are calculated as

$$X = \frac{\sum_{\lambda} E_{\lambda} x_{\lambda} R(\lambda)}{\sum_{\lambda} E_{\lambda} x_{\lambda}}, \quad Y = \frac{\sum_{\lambda} E_{\lambda} y_{\lambda} R(\lambda)}{\sum_{\lambda} E_{\lambda} y_{\lambda}} \quad \text{and} \quad Z = \frac{\sum_{\lambda} E_{\lambda} z_{\lambda} R(\lambda)}{\sum_{\lambda} E_{\lambda} z_{\lambda}}, \quad (5)$$

where  $E_{\lambda}$  denotes the spectral distribution of the illuminating source and  $R(\lambda)$  the measured spectral reflectance distribution of the object. The tristimulus functions  $x_{\lambda}$ ,  $y_{\lambda}$  and  $z_{\lambda}$  represent the sensitivity of the receptors. The  $XYZ$ -plane is not very uniform and also distorted with regard to hue and chroma. The CIELAB system offers an improved color space, which is well suited for absorbing media such as tissue. In CIELAB, the tristimulus values are transformed into a color specification by the psychometric brightness  $L^*$  and the color hue coordinates  $a^*$  and  $b^*$  by

$$L^* = 116 \sqrt[3]{\frac{Y}{Y_n}} - 16, \quad a^* = 500 \left( \sqrt[3]{\frac{X}{X_n}} - \sqrt[3]{\frac{Y}{Y_n}} \right) \quad \text{and} \quad b^* = 500 \left( \sqrt[3]{\frac{Y}{Y_n}} - \sqrt[3]{\frac{Z}{Z_n}} \right). \quad (6)$$

Here,  $X_n$ ,  $Y_n$  and  $Z_n$  denote the color values for a white standard, usually D65. As the laser scanning endoscope can measure only  $R(\lambda_1)$ ,  $R(\lambda_2)$  and  $R(\lambda_3)$  for three wavelengths  $\lambda_1$ ,  $\lambda_2$  and  $\lambda_3$ , the continuous spectral reflectance  $R(\lambda)$  will not be available so that an exact color measurement is not possible.

Nevertheless, one can try to minimize the difference between the color  $\vec{C} = (L^*, a^*, b^*)$  derived from the measurement of  $\vec{R} = (R(\lambda_1), R(\lambda_2), R(\lambda_3))$  and the correct color  $\vec{C}_0 = (L_0^*, a_0^*, b_0^*)$  defined by the continuous spectral reflectance  $R(\lambda)$  according to equations 5 and 6. The idea is to find a linear transformation

$$\vec{C} = \mathbf{A} \vec{R} + \vec{B}, \quad (7)$$



for which the difference  $\|\vec{C} - \vec{C}_0\|$  is minimal for the measurements of  $\vec{R}$  made with the endoscope. Therefore, a transformation has to be determined suitable for a wide class of different tissue types.

To determine  $\vec{A}$  and  $\vec{B}$ , the spectra for eight different visceral organs commonly under observation during endoscopic or laparoscopic surgery were recorded (figure 9, left). Among them were bladder, kidney, liver, colon and bowel. The data was acquired *in vivo* during an animal lab using a fiber based spectrometer equipped with a xenon light source. Illumination and detection were not perpendicular to the tissue surface to avoid reflection from the tissue. A least squares fit on the data was performed to derive  $\vec{A}$  and  $\vec{B}$  while minimizing  $\|\vec{C} - \vec{C}_0\|$ . Apart from using  $\vec{R} = (R(\lambda_1), R(\lambda_2), R(\lambda_3))$  for a three color system, the fit was performed for a two color system with  $\vec{R} = (R(\lambda_1), R(\lambda_2))$ . One wavelength was omitted, since tissue colors are in the red region mostly. Being able to omit one color without significantly losing color information would make sense to reduce system complexity and costs.

For the eight tissue types, the  $L^*a^*b^*$ -color derived from the spectrum were found to be similar compared to the  $L^*a^*b^*$ -color derived from two or three discrete wavelengths found through the fit (figure 9, right). The matching is better for the three color system than for the two color system. The differences do not exceed the usual color calibration variations found between different video cameras. Actually the wavelengths found with the two-color-fit correspond well to the green and red wavelengths of the three-color-fit, so in fact one could afford to omit a blue wavelength for standard gastrointestinal imaging.

However, this can not be regarded as a general proof for a satisfying color reproduction, since pathological spectra can be constructed, for which the scanner would obviously not work. For example, if the spectrum had a gap around one detecting wavelength, the color measured with the device would differ a lot from the color perceived by the brain based on the continuous spectrum. In general, metameric pairs will not necessarily be measured as the same color with the laser scanning endoscope.

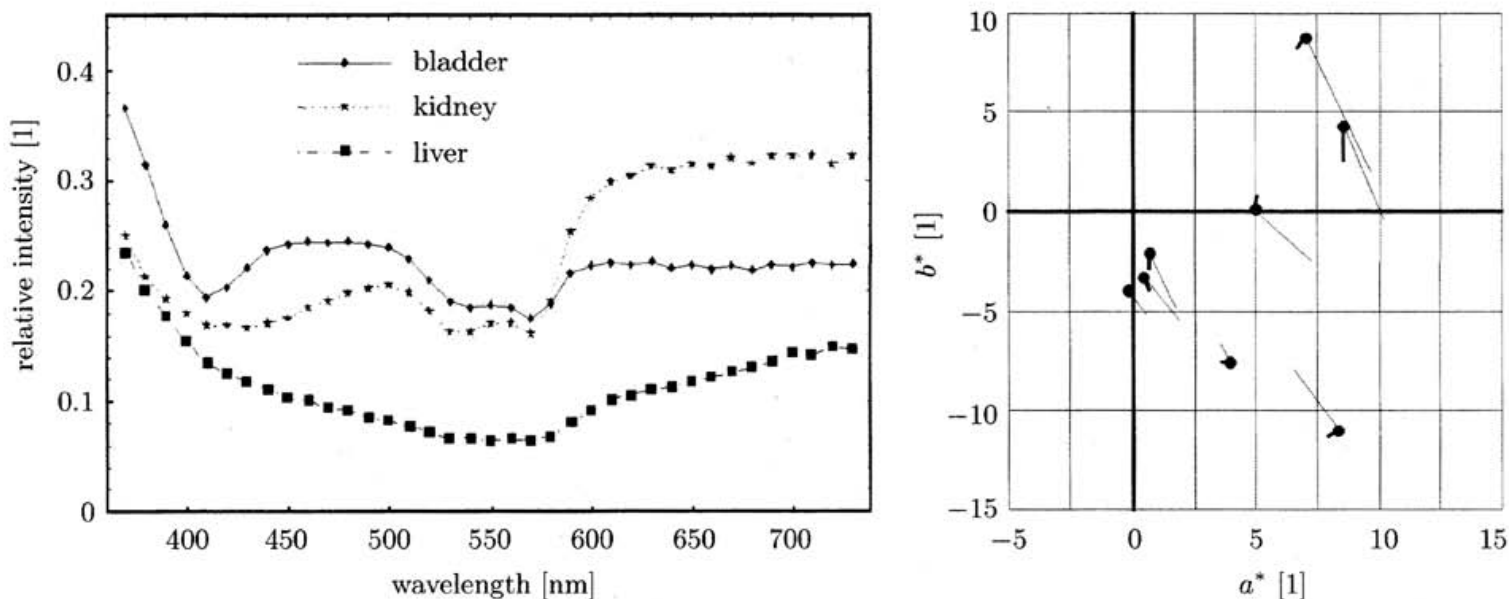


**Figure 9.** Left: Examples of spectroscopy results for bladder, kidney and liver tissue. Right: Color reproduction errors made when using discrete wavelengths of the spectrum for 8 tissue types. The filled circles represent the color  $\vec{C}_0$  of the tissue in the  $a^*-b^*$ -plane as measured with the spectrometer. The thick and thin lines connect these color values with those obtained by least squares fit for three or two discrete wavelengths. As expected, the error made is smaller when three wavelengths are employed.

## 4.2. Expert System for the Detection of Lesions

Tissue microstructures located on the colonic mucosal surface, such as pit patterns,<sup>8</sup> can be used for medical diagnosis. The laser scanning endoscope is capable of resolving structures of this size at working distances significantly longer than those of magnifying video endoscopes. To enable automatic analysis of the endoscopic



images, an expert system with an interface to the image acquisition software was implemented. This system can augment the accuracy of the diagnostic procedure performed by the medical professional.

The expert system consists of a multilayer feed-forward neural network.<sup>9</sup> In a neural network learning replaces *a priori* program development, i.e. the functionality is developed by training on sample data. Training was performed using still images and frame sequences taken from video sequences of various colonoscopies.

Specific image features are evaluated by the neural network to identify areas that are of suspicious pathology. Different feature extraction techniques are used for the description of the textural content of the examined regions, including the estimation of cooccurrence and run-length measures. These techniques are applied on the spatial as well as on the wavelet domain of the acquired colonoscopic video frames. The wavelet transform is offered by the implemented software and results in a multiresolution representation of the images which usually enhances the inherent textural information.

The entire system was tested using various combinations of texture features and different training frames for a number of video sequences containing small lesions. Among the methods used, the textural characteristics of the lesions were described best by four cooccurrence matrix features in the wavelet domain, namely angular second moment, correlation, inverse difference moment and entropy. The results are found to be very promising not only for the high percentage of successful recognitions but also for the ability to localize the lesion among the different frames (figure 10). A percentage of successful recognitions exceeding 93% on average per frame sequence has been achieved for all of the frame sequences.

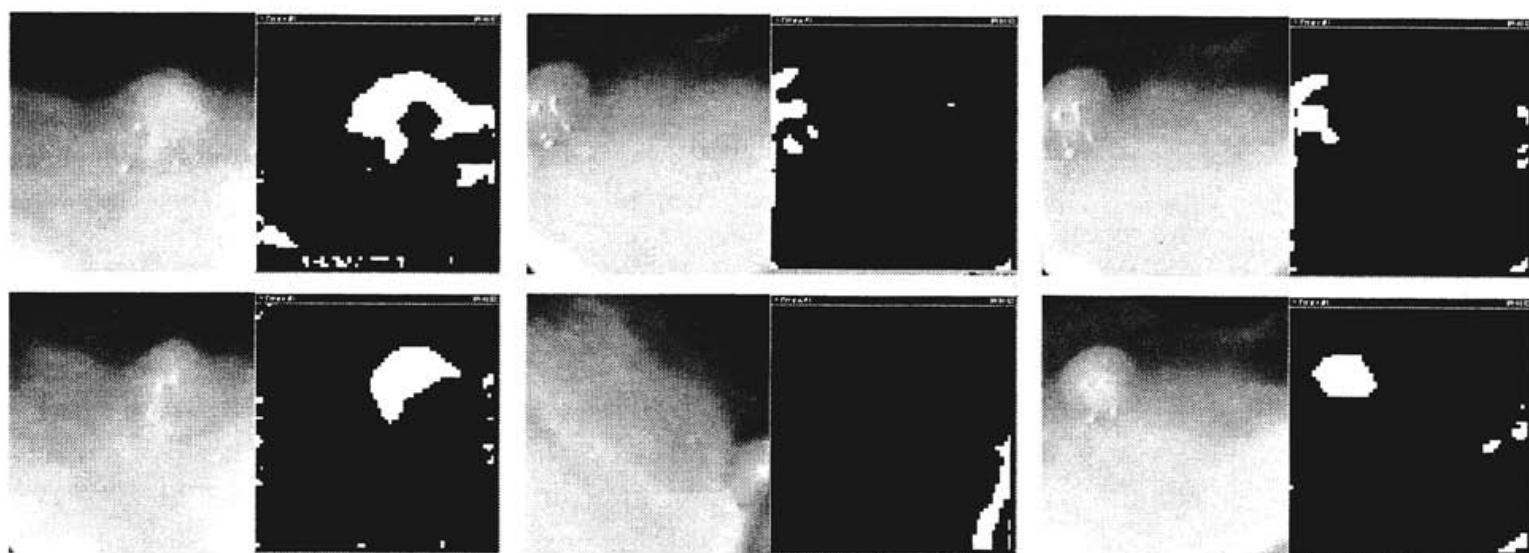


**Figure 10.** Representative evaluation of colonoscopic video frames by the neural network expert system. The analysis was based on the four cooccurrence matrix features in the wavelet domain which are mentioned in the text. The 1 bit black and white frames correspond to the expert system's output. The white areas designate the recognized lesions.

## 5. DISCUSSION AND CONCLUSIONS

A fully operational color laser scanning endoscope prototype has been designed, assembled and tested. It offers enhanced resolution compared to CCD or CMOS based devices at working distances common in endoscopy. The use of lasers for illumination makes the device principally multi-functional, as different diagnostic image formation processes could be employed. The scanning approach is mainly responsible for the high resolution, since the single point illumination makes the device at least semi-confocal. Therefore, the contrast generation at the sample is far superior compared to modern endoscopy techniques which use wide field illumination. Because of the low numerical aperture, only a small portion of the backscattered light can be collected which reduces contrast and signal-to-noise ratio significantly. Hence, it must be doubted whether early lesions will be detectable based on the backscattering signal alone. In addition, the field of view is limited by the achievable deflections of the scanning mirrors. Therefore, the device cannot substitute modern video endoscopes. Nevertheless, now a means for endoscopic laser scanning imaging is available which could be used for many diagnostic laser applications

discussed today. Photodynamic, fluorescence life time, laser-induced fluorescence or auto-fluorescence imaging could be performed.

For real endoscopic use, the system would have to be upgraded to contain a focusing mechanism, which could be realized by moving the ends of the optical fibers inside the endoscope head axially. Should an enlargement of the field of view not become available, a camera module for surround view would have to be added as well. Technically, a gimbaled scanning mirror<sup>10,11</sup> could enhance the scanning mechanism, which would reduce both the size of the device and also the losses due to scattering, mirror surface absorption and wavefront deformation.

Principally a satisfying color reproduction can be achieved by measuring the sample spectrum at only three points. Is the application regime limited to the reddish gastrointestinal surfaces, even only two laser wavelengths would come close to this result. This could be even valid for an application in chromoendoscopy, given that the two wavelengths are chosen as described.

The neural network approach to provide an expert system for medical decision-making delivered promising results which are independent of the performance of the laser scanning endoscope. The expert system can be trained on video sequences, although sequences provided by the laser scanning endoscope should principally contain more texture and thus yield even better results. In the long run, neural networks might become a standard feature of image processors for endoscopy. However, the final diagnostic decision must be undoubtedly left to the medical expert who is the only person eligible to evaluate the proposal made by the system.

## ACKNOWLEDGMENTS

This work has been supported by the Commission of the European Communities as the part "MEDEA – Micro-scanning Endoscope with Diagnostic and Enhanced Resolution Attributes" of the European Project BIOMED2 under contract number BMH4-CT97-2399. The authors also appreciate the efforts of G. Anagnostopoulos, S. A. Karkanis, P. Dario, C. Stefanini, G. Delacrétaiz, B. Wagner, K. Dörschel, R. Schütz, J. Knittel and W. Junger for their contributions to make the project succeed. For training and testing the neural network, we are especially grateful for having been able to access the rich library of high quality gastrointestinal images of K. E. Grund of the Surgical Endoscopy Department at University of Tübingen.

## REFERENCES

1. T. Lange, "State of the art of video techniques for endoscopic surgery," *Endosc. Surg. Allied Technol.* **1**, pp. 29–35, 1993.
2. A. Cuschieri, G. Buess, and J. Perissat, *Operative Manual of Endoscopic Surgery*, Springer, Heidelberg, 1992.
3. K. E. Petersen, "Silicon torsional scanning mirror," *IBM J. Res. Dev.* **24**, pp. 631–637, 1980.
4. D. Dickensheets and G. Kino, "Silicon-micromachined scanning confocal optical microscope," *IEEE J. Microelectromech. Syst.* **7**, pp. 38–47, 1998.
5. U. Hofmann, S. Mühlmann, M. Witt, K. Dörschel, R. Schütz, and B. Wagner, "Electrostatically driven micromirrors for a miniaturized confocal laser scanning microscope," in *Miniaturized Systems with Micro-Optics and MEMS, Proc. SPIE 3878*, pp. 29–38, (Santa Clara), 1999.
6. T. Farrell, M. Patterson, and B. Wilson, "A diffusion theory model of spatially resolved, steady-state diffuse reflectance for the non-invasive determination of tissue optical properties in vivo," *Med. Phys.* **19**(4), pp. 879–888, 1992.
7. H. Kang, *Digital Color Halftoning*, SPIE Press, Washington, 1999.
8. S. Kudo, S. Tamura, T. Nakajima, H. Yamano, H. Kusaka, and H. Watanabe, "Diagnosis of colorectal tumorous lesions by magnifying endoscopy," *Gastrointest. Endosc.* **44**(8–14), 1996.
9. C. Bishop, *Neural Networks for Pattern Recognition*, Oxford University Press, Oxford, 1995.
10. D. L. Dickensheets and G. S. Kino, "Miniature scanning confocal microscope." Stanford University, Patent (USA) 6 088 145, 2000.
11. M. George, L. Schnieder, and G. Buess, "Confocal device and application strategies for endoluminal optical coherence microscopy," in *Optical Coherence Tomography and Coherence Techniques*, W. Drexler, ed., *Proc. SPIE 5140*, (Munich), 2003.